Clays and Clay Minerals, Vol. 64, No. 4, 401–412, 2016.

STRUCTURAL AND SPECTROSCOPIC CHARACTERIZATION OF MONTMORILLONITE INTERCALATED WITH *N*-BUTYLAMMONIUM CATIONS ($N = 1-4$) – MODELING AND EXPERIMENTAL STUDY

EVA SCHOLTZOVÁ[1,*], JANA MADEJOVÁ[1], L'UBOŠ JANKOVIČ[1], AND DANIEL TUNEGA[2]

[1] Institute of Inorganic Chemistry of Slovak Academy of Sciences, Dúbravská cesta 9, 845 36 Bratislava, Slovakia
[2] Institute for Soil Research, University of Natural Resources and Life Sciences, Peter-Jordan-Strasse 82b, Vienna, A-1190, Austria

Abstract—A detailed structural characterization of organo-clays is a key in understanding their properties. In this work, mono-, di-, tri-, and tetra-butylammonium (*n*BA; $n = 1-4$) cations intercalated in the layered clay mineral montmorillonite (Mnt) have been studied for the first time by combining a theoretical approach based on density functional theory (DFT) and infrared spectroscopy. The DFT calculations revealed the detailed structure and position of *n*BA cations in the interlayer space. A relation between the basal spacing (d_{001} parameter) and the cation size and structure was found, and explained with respect to the structure, composition, and size of the organic cations. Hydrogen bonds between $-NH_x$/$-CH_3$/$-CH_2$ groups of the *n*BA cations and oxygen atoms of the basal planes of the Mnt layers were found to be an important factor for the arrangement and energetic stabilization of cations in the interlayer space. The N–H···O hydrogen bonds are stronger than C–H···O hydrogen bonds and the stabilization decreases with decreased number of bands. Analysis of DFT-calculated vibrational modes helped in understanding a problematic region of the experimental infrared spectra (4000–3000 cm^{-1}), in which assignment of all vibrational modes unambiguously was not possible because of a significant overlap of broad bands.

Key Words—Butylammonium Cations, DFT, FTIR, Hydrogen Bonds, Interaction Energy, Modeling, Montmorillonite.

INTRODUCTION

The production of organo-clays from montmorillonite, the most important clay mineral of the smectite group, has attracted much attention from researchers because of prospective application of these materials in various areas, *e.g.* as adsorbents of organic contaminants from waste water, as catalysts for reactions using non-polar substrates, or as reinforcing fillers in composites with polymers (Theng, 1974; Ruiz-Hitzky and Van Meerbeek, 2006; de Paiva *et al.*, 2008; Guegan, 2010, 2013; Seyidoğlu and Yilmazer, 2013). Natural smectites are predominantly hydrophilic, due mainly to hydration of inorganic exchangeable cations that compensate the negative layer charge due to isomorphic substitutions in the tetrahedral and/or octahedral sheets. Although natural smectites have a high sorption affinity for cations, the ability to adsorb weakly polar, non-polar, and anionic species in the interlayer space and/or on the clay surface is limited. Modifying the surface hydrophilic/hydrophobic ratio, *e.g.* by intercalating organic, most often quaternary ammonium cations, into the interlayer space can enhance the capacity of smectites to retain these species (Raussell-Colom and Serratosa, 1987; Kukkadapu and Boyd, 1995; Lagaly *et al.*, 2006; He *et al.*, 2014).

Small quaternary alkylammonium cations are often used to modify the surfaces of clay minerals for better adsorption of neutral organic contaminants (Lee *et al.*, 1990; Chun *et al.*, 2003). For example, tetramethylammonium (TMA) and tetramethylphosphonium (TMP) modified smectites have been examined as possible adsorbents for chlorinated phenols from water. The TMP-smectite was a better sorbent than TMA-smectite, which did not measurably adsorb any of the phenolic compounds. This disparity in sorption efficiency was attributed to differences in hydration of the interlayer cations (Lawrence *et al.*, 1998). Water inhibits sorption of neutral organic compounds on montmorillonites saturated with small alkylammonium cations. An infrared study was, therefore, conducted to follow the interaction of water with TMA- and trimethylphenylammonium (TMPA) montmorillonites. The results showed that water preferentially hydrates TMA and TMPA cations, rather than the siloxane surface of montmorillonite (Stevens and Anderson, 1996).

Changes in the adsorption properties of kaolinite and montmorillonite modified with tetrabutylammonium (TBA) ions have been previously reported with respect to cations such as Pb(II) (Sen Gupta and Bhattacharyya,

* E-mail address of corresponding author:
Eva.Scholtzova@savba.sk
DOI: 10.1346/CCMN.2016.0640404

This paper is published as part of a special issue on the subject of 'Computational Molecular Modeling'. Some of the papers were presented during the 2015 Clay Minerals Society-Euroclay Conference held in Edinburgh, UK.

2005), Cd(II) (Sen Gupta and Bhattacharyya, 2006), and Cu(II) (Bhattacharyya and Sen Gupta, 2006). The organo-clays, TBA-kaolinite and TBA-montmorillonite, were also used for adsorption of Fe(III), Co(II), and Ni(II) cations from aqueous solution under different conditions of p*H*, time, and temperature (Bhattacharyya and Sen Gupta, 2009). Organo-clays prepared from montmorillonite saturated with cetyltrimethylammonium (*i.e.* hexadecyl trimethylammonium) bromide and tetrabutylammonium bromide were used to catalyze the production of glycerol monolaurate (Wibowo *et al.*, 2010). The alkylammonium ions can also act as phase-transfer catalysts to accelerate a slow reaction stemming from poor interaction between the reactants (Ghiaci *et al.*, 2003). The size and the amount of alkylammonium cations, the intensity of acid treatment, and the type of clay mineral significantly influence the extent of organo-clay dissolution (Breen *et al.*, 1997). Comparison of organic cations containing one long alkyl chain (*e.g.* hexadecyltrimethylammonium) with tetramethylammonium showed a higher catalytic activity of materials with the smaller TMA cation.

Organo-clays are routinely studied by X-ray diffraction (XRD) methods. In addition to XRD analysis, spectroscopic research on organo-clays, *e.g.* by infrared (IR), Raman (Vaia *et al.*, 1994; Yariv, 2001; He *et al.*, 2004; Zhu *et al.*, 2005; Frost *et al.*, 2008; Madejová *et al.*, 2010; Jankovič *et al.*, 2015), or ultraviolet−visible spectroscopy (Czimerova *et al.*, 2009), can also provide information about the structure and properties of organo-clays. Infrared spectroscopy was found to be useful in studies of acid-treated organo-clays prepared as potential catalysts (Breen *et al.*, 1997; Madejová *et al.*, 2012). The stability of montmorillonites intercalated with quaternary short alkyl-chain cations (TMA, tetraethyl (TEA), tetrapropyl (TPA), and tetrabutyl (TBA) in HCl was studied by different analytical techniques, including IR spectroscopy, in the near-IR region (NIR) because of potential application of organo-clays as acid catalysts (Pálková *et al.*, 2011; Madejová *et al.*, 2012; Palkova *et al.*, 2013). Experimental XRD and spectroscopic data are, however, often unable to provide comprehensive answers to questions related to, for example, the detailed arrangement or the nature of organic cation interactions in the interlayer spaces or on the surfaces of clay minerals.

The use of theoretical computational methods and molecular simulations can effectively complement experimental data. These methods range from quantum-chemical to molecular mechanics (based on sets of empirically derived interatomic potentials, called Force Fields (FF)), often in combination with classical molecular dynamics (MD) or Monte Carlo (MC) methods (Teppen *et al.*, 1998; Heinz *et al.*, 2005). The simulations can predict the distribution and orientation of molecules in the interlayer space and on the surface, the bonding relations in organo-clays (Scholtzova *et al.*, 2008; Scholtzova and Smrcok, 2009), or the character of interactions between layer and interlayer host species. In addition, calculating spectroscopic parameters is also possible helping significantly in the interpretation of complex experimental spectra (Hafner, 2003). For example, a good agreement with experimental data was achieved for the relationship between interlayer space height and intercalated cation size which was predicted by classical FF simulations (Heinz *et al.*, 2007; Fu and Heinz, 2010a). The MD simulations were performed in order to study ethylene glycol interactions with smectite (Szczerba *et al.*, 2014), in a study of the crystalline swelling behavior of montmorillonites with different interlayer Na^+ and Ca^{2+} ion compositions, and temperature and pressure effects on the swelling behavior (Sun *et al.*, 2015). Examples of the MC method are studies of montmorillonite intercalated with the tetraphenylphosphonium cation which has a high sorption ability for acetocholor (Aggarwal *et al.*, 2007), and of surface coverage effects and alkyl chain length *n* on alkyltrimethylammonium chloride (C(*n*)TMA)Cl aggregate structures assembled on the montmorillonite-water interface (Klebow and Meleshyn, 2012).

The results presented in a previous study (Madejová *et al.*, 2012) raise an interesting question by comparing experimental IR data for montmorillonite intercalated with TMA-, TEA-, TPA-, and TBA- cations with quantum chemical calculated data based on density functional theory (Scholtzová *et al.*, 2013; Scholtzová *et al.*, 2014). These theoretical results provided information on the arrangement and bonding of tetraalkylammonium cations in the montmorillonite interlayer space. The calculated vibrational spectra helped in the interpretation of the experimental IR spectra, specifically in distinguishing the stretching modes of the $-CH_3$ and $-CH_2$ groups. In those works, all the organo-clays studied contained small cations with four identical alkyl chains bonded to a nitrogen head. Thus, only the interactions of the $-CH_3$ and/or $-CH_2$ groups with the montmorillonite layer were considered. A different situation, however, may arise if some of the alkyl chains are substituted with protons, *i.e.* if the cation also contains $-NH_3$, $=NH_2$ or $\equiv NH$ head groups. The aim of this study was, therefore, to explore the structure, interactions, and vibrations of several short *n*-butylammonium (n = 1−4) cations in the interlayer space of montmorillonite, and to study the stability of the organo-clays at the molecular level by a combination of DFT calculations and infrared measurement. This approach has principally yielded, in this present work, interpretation of the NH and CH stretching bands in the experimental mid-IR spectra by means of the DFT-calculated vibrational density of states.

MATERIALS AND METHODS

Experimental details

Montmorillonite (SAz) was separated from the bentonite SAz-1 (Cheto, Arizona, USA), obtained from

https://doi.org/10.1346/CCMN.2016.0640404 Published online by Cambridge University Press

the Source Clays Repository of The Clay Minerals Society. The clay was suspended in distilled water, Na-saturated by repeated treatment with 1 M NaCl, and <2 μm fractions were collected. The excess ions were removed by washing with distilled water. The prepared NaMnt (determined structural formula $[Si_{8.00}][Al_{2.59}Fe_{0.16}Mg_{1.26}]Na_{1.14}Ca_{0.03}K_{0.01}O_{20}(OH)_4.nH_2O$) was dried at 60ºC and ground to pass a 0.2 mm sieve. A cation exchange capacity (CEC) of 1.2 mmol g^{-1} was obtained using the Cu-trien method (Pálková *et al.*, 2011). All chemicals (*n*-butylamine, dibutylamine, tributylamine, tetrabutylammonium bromide, hydrogen bromide, cyclohexane, and *n*-propanol) were obtained from Sigma-Aldrich (St. Louis, Missouri, USA).

Mono-, di-, and tri-butylammonium bromides were prepared by reaction of anhydrous hydrogen bromide (HBr) gas with the corresponding free amine dissolved in cyclohexane. The solution of the pure butylamine in cyclohexane (0.1 M) was prepared in a 250 mL three-necked flask equipped with a mechanical stirrer, an immersion thermometer, and a glass inlet tube. The flask and its contents were cooled to 5ºC in an ice bath and pure gaseous HBr was slowly introduced into the flask at a rate such that the reaction temperature did not exceed 10ºC. On completion of the HBr addition, the reaction mixture was stirred for 10 min. After completion of the addition, the ice bath was removed and the product was isolated by filtration through a 50 mL medium-porosity sintered-glass funnel. The filtrate was washed with dried cyclohexane. Further purification was achieved by recrystallization from *n*-propanol.

For the preparation of all butylammonium-montmorillonite samples (*n*BAMnt), the solvent intercalation process was used. One gram of sodium montmorillonite (NaMnt) was added to 100 mL of distilled water and the suspension was stirred for 24 h at room temperature to ensure the NaMnt was adequately dispersed. Subsequently, a calculated volume (equal to the CEC of NaMnt) of a 1% aqueous solution of butylammonium bromide was slowly added (1 mL min^{-1}) to the suspension and the mixture was vigorously stirred for 24 h at laboratory temperature (~25ºC).

After the reaction, the suspension was centrifuged and the final product was washed by centrifugation five times with 250 cm^3 of distilled water to remove excess amounts of water-soluble butylammonium and inorganic (NaBr) salts. Saturation with *n*BABr was repeated three times in order to achieve the highest possible loading.

Colloidal dispersions of organo-clays were mounted by suction onto glass slides, air dried for 3 h, and mounts with the oriented clay film were transferred to a desiccator over a saturated solution of $Mg(NO_3)_2$ for equilibration at 54% relative humidity prior to XRD analysis.

The X-ray powder diffraction data were collected on a D8 Advance Bruker diffractometer (Bruker AXS GmbH, Karlsruhe, Germany) using CuKα (40 kV, 40 mA, λ = 1.541 78 Å) radiation and a diffracted beam graphite monochromator. The patterns were recorded in the range of 1.5−72º (2θ) using a step of 0.05º2θ. In Bragg-Brentano geometry (Theta-2Theta), a 1.0 mm divergent slit, a 1.0 mm detector slit, and a 6.0 mm antiscatter slit were used.

The IR spectra were collected with a Nicolet 6700 Fourier Transform Infrared (FTIR) spectrometer from Thermo Fisher Scientific, Inc. (Madison, Wisconsin, USA). The KBr pressed disk technique (1 mg of sample and 200 mg KBr) was used to measure spectra in the mid-infrared region (4000-400 cm^{-1}). The pellets were heated overnight at 120ºC to minimize the amount of adsorbed water on the KBr and/or outer montmorillonite surfaces. During measurement, the instrument was continually purged with dry air. For each sample, 64 scans were recorded with a 4-cm^{-1} resolution. Spectral manipulations were performed using the Thermo Scientific OMNIC" software package. To compare the intensities of the CH stretching bands, the spectra were normalized to the Si−O stretching band of montmorillonite near 1030 cm^{-1}.

Structural models

The compositional variety and structural complexity of clay minerals usually require a certain level of simplification when constructing a model for use in molecular simulations, especially when quantum chemical methods are involved. Owing to a lack of complete structural data for the SAz-1 montmorillonite used in the experiment, structural models for the calculations were derived from the monoclinic structure of Wyoming montmorillonite with a structural formula of $Na_{0.75}(Al_{3.5}Mg_{0.5})(Si_{7.75}Al_{0.25})O_{20}(OH)_4 \cdot nH_2O$ (Tsipurski, 1984). The structural models used in the calculations have the simplified composition of Wyoming montmorillonite, only with Mg^{2+} substituted for Al^{3+} and without the presence of Fe^{3+} cations in the octahedral sheets. This simplification is consistent with the composition of the SAz-1 montmorillonite used for organo-clay preparation in this work. Similar models with the same clay composition have also been used in theoretical studies of this montmorillonite intercalated with TMA- (Scholtzová *et al.*, 2013), TEA-, TPA-, and TBA-cations (Scholtzová *et al.*, 2014).

Owing to the size of the organic cations, computational cells for the *n*BAMnt models have a size of 4*a*4*bc* of the montmorillonite elementary cell with final lattice vectors *a* = 20.966 Å, *b* = 18.176 Å, and *c* = 20.7 Å (summary formula was $MgAl_{31}Si_{64}O_{192}H_{32}$). Two initial configurations were used for the *4*BA cation in the previous simulations of *4*BAMnt intercalate (Scholtzová *et al.*, 2014): one with the cation in a quasi-planar configuration in an interlayer space corresponding to the minimal (MIN) interlayer distance (Figure 1a), and the second with the cation in a configuration corresponding to the maximal d_{001} spacing (MAX) (Figure 1b).

https://doi.org/10.1346/CCMN.2016.0640404 Published online by Cambridge University Press

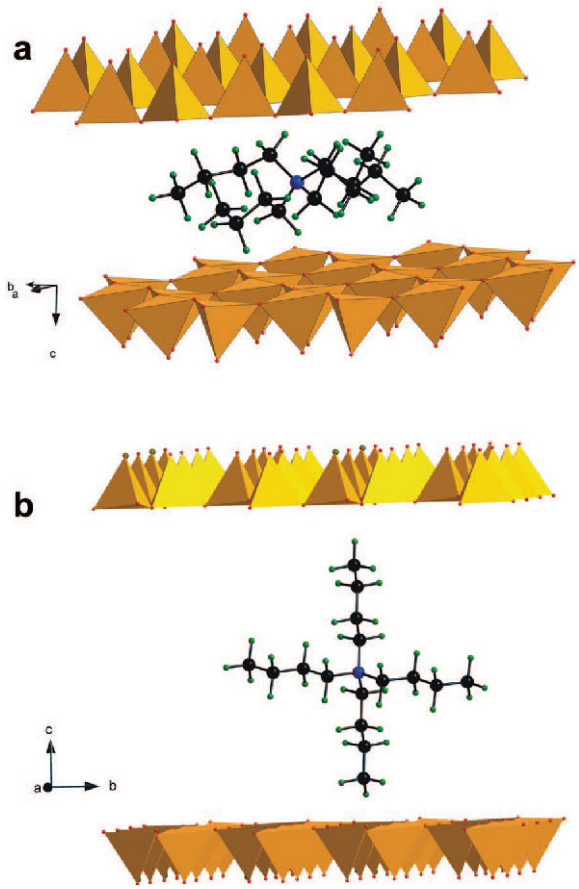

Figure 1. Initial configurations of *4*BA cation in the interlayer space of montmorillonite: (a) quasi-planar structure (MIN), (b) tetrahedral structure (MAX).

Geometric optimizations on both models converged to identical structures with a quasi-parallel (with respect to the layer surface) arrangement of the butylammonium (BA) chains. Only a parallel initial configuration of BA chains, therefore, was used in the construction of the models of *1*–*3*BAMnt (Figure 1a). The structure of the *2*BA cation was placed in two planar configurations (*cis* and *trans*, Figures 2a, b) in the interlayer space.

Computational details

The DFT calculations were performed using the Vienna *Ab Initio* Simulation Package (VASP) program (Kresse and Hafner, 1993; Kresse and Furthmuller, 1996). The exchange-correlation energy was expressed in the framework of the generalized gradient approximation (GGA) using the DFT functional proposed by Perdew, Burke, and Ernzerhof (PBE) (Perdew *et al.*, 1996). The Kohn-Sham equations were solved by applying the variational method (mathematical interative algorithm) using a plane-wave (PW) basis set with an energy cutoff of 500 eV. The electron–ion interactions were described using the projector-augmented-wave (PAW) method (Blochl, 1994; Kresse and Joubert, 1999). Brillouin-zone sampling was restricted to the *gamma*-point alone due to the large computational cells. Structural relaxation was performed in two steps. Firstly, all atomic positions were relaxed while keeping the unit cell fixed. Secondly, the atomic positions were relaxed together with the unit cell parameters. No symmetry restrictions were applied during any relaxation procedure. The relaxation criteria were 10^{-5} eV/atom for the total energy change, and 0.005 eV/Å for the maximum force acting on any atom.

Normal modes of vibrations were calculated within the fixed optimized cells using a finite difference method, and normal mode analysis was performed within the harmonic approximation. The Hessian was constructed from single-point energy calculations on the 6*n* structures generated from the optimized structures by displacing each of the *n* atoms in the cell in a positive and negative direction along the three Cartesian directions *x, y*, and *z* (Hafner, 2003).

RESULTS AND DISCUSSION

Structural relaxation

Unfortunately, obtaining complete structural data of organo-clays from the powder XRD method is practically impossible; therefore, only the d_{001} spacing was determined from the XRD patterns of the *n*BAMnt samples (Table 1). The geometric optimization of the *n*BAMnt models provided optimized unit-cell parameters and d_{001} values (Table 1).

In the case of the two proposed models for an intercalated cation with two butyl $-C_4H_9$ chains, the d_{001} value of the *2*BAMnt *cis* model (13.50 Å) was in better agreement with the experimental one (13.56 Å) than the value for the *2*BAMnt *trans* model (12.97 Å).

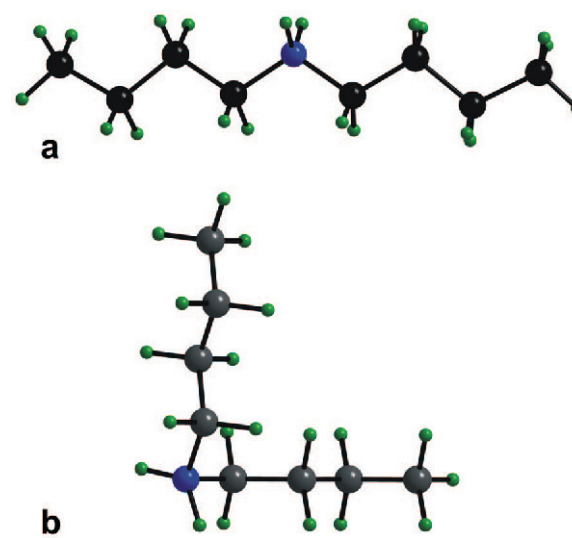

Figure 2. Initial configurations of *2*BA cation: (a) *cis*, (b) *trans*.

https://doi.org/10.1346/CCMN.2016.0640404 Published online by Cambridge University Press

Table 1. DFT-optimized structural parameters (*a, b, c,* α, β, γ−cell parameters (Å, º), d_{001} − basal spacing (Å]), ΔE_r − interaction energy (kJ/mol) of *n*BAMnt models (*n* = 1−4). opt − optimized, exp − experimental.

Model	*a*	*b*	*c*	α	β	γ	d_{001_opt}	d_{001_exp}	ΔE_r
*1*BAMnt	20.897	18.117	12.896	89.7	96.9	90.0	12.80	13.23	–120.87
*2*BAMnt$_{cis}$	20.887	18.105	13.547	90.2	85.5	90.0	13.50	13.56	–101.38
*2*BAMnt$_{trans}$	20.890	18.105	12.969	88.8	90.7	90.0	12.97		–100.98
*3*BAMnt	20.888	18.103	13.707	91.8	94.7	90.0	13.65	13.74	–73.53
*4*BAMnt	20.911	18.132	15.585	90.2	93.9	90.0	15.55	16.60	–21.20

The comparison of the total electronic energies of both *2*BAMnt models favors the *cis* model by 66 kJ/mol in comparison to the *trans* configuration. This finding suggests, thus, that the *cis* configuration is preferred in the interlayer space and it also agrees with the better match between calculated and experimental d_{001} spacing for the *cis* model.

The *a*- and *b*-lattice vectors of all models were almost unaffected by cation size, and the optimized *a* and *b* values were almost identical (Table 1). As expected, the *c* vector extends on increasing the cation size, but this increase is not substantial except in the case of the *4*BAMnt model. The optimized structures had BA chains in a configuration parallel to the basal surfaces of the montmorillonite layers (Figure 3). The calculated d_{001} spacing values correlate very well with the experimental data. The interlayer expansion in the *1*BAMnt, *2*BAMnt, and *3*BAMnt samples was only ~1−1.5 Å compared to the original Na-montmorillonite (12.53 Å calculated at the PBE DFT level for the montmorillonite model intercalated with $[Na(H_2O)_6]^+$ (Berghout *et al.*, 2010)). A similar parallel arrangement was also observed for tetraalkylammonium cations with short alkylammonium chains (C = 2−4) (Scholtzová *et al.*, 2014). Both the calculated and experimental d_{001} spacings (Table 1) indicate an expansion of the interlayer space for TBA cations. The cations with *1*−*3*BA chains have polar NH bonds in a cationic head that occupies a relatively small volume. In contrast, the *4*BA cation has four large non-polar aliphatic chains, which takes up a large space in the interlayer galleries. Moreover, the interactions of the aliphatic chains are generally of a weak dispersive nature and the $-CH_3/-CH_2$ groups form weaker hydrogen bonds with the surface oxygen atoms of the montmorillonite layer than the NH bonds (details are discussed later). The cations in the models *1*−*3*BAMnt,

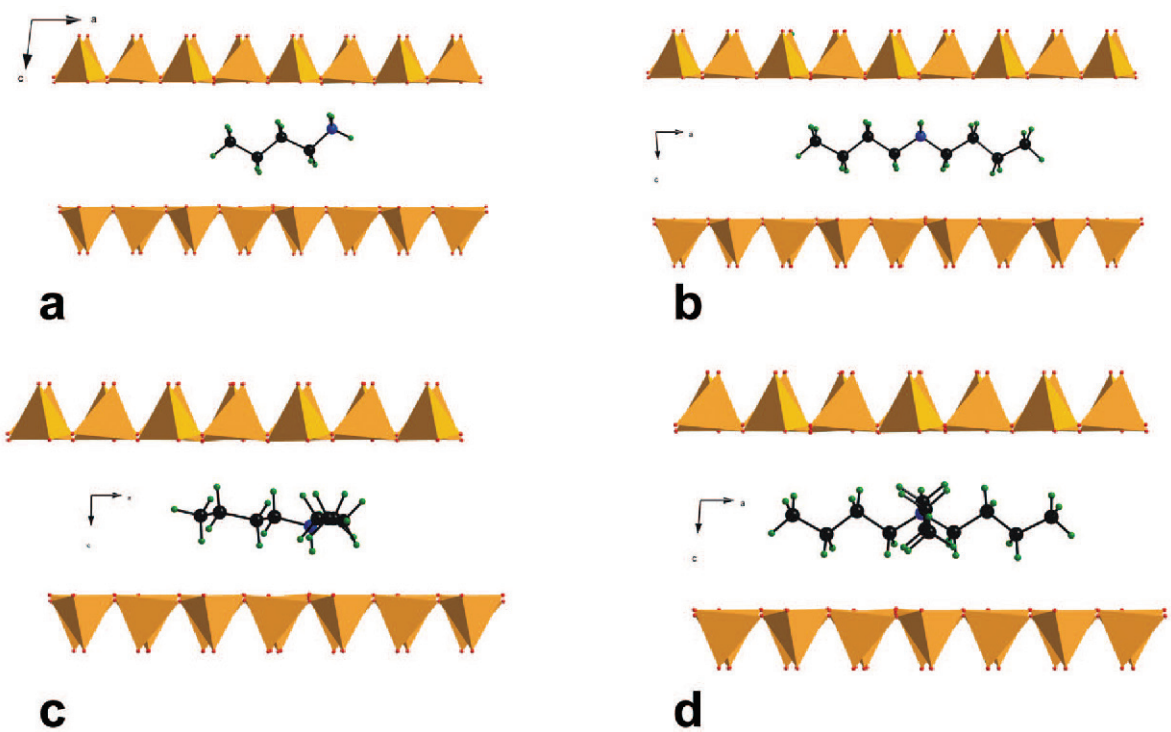

Figure 3. DFT-optimized structures of (a) *1*BAMnt, (b) *2*BAMnt *cis*, (c) *2*BAMnt *trans*, and (d) *3*BAMnt models.

https://doi.org/10.1346/CCMN.2016.0640404 Published online by Cambridge University Press

therefore, were sandwiched more tightly by the montmorillonite layers than in the *4*BAMnt model, as was reflected in the larger d_{001} spacing of the *4*BAMnt model.

Hydrogen bonds and energetic stability

Although the basic interactions between intercalated cations and negatively charged montmorillonite layers are of an electrostatic nature, hydrogen bonds and dispersion interactions also play an important role in interlayer cation stabilization. The analysis of the optimized models showed that the intercalated *n*BA cations were anchored in the interlayer space by two types of hydrogen bonds with basal oxygen atoms as proton acceptors – N−H···O and C−H···O (Table 2), which both could be classified as of moderate-to-weak strength (Desiraju and Steiner, 2006).

In the *1*−*3*BAMnt models the N−H···O hydrogen bonds were a little stronger than those formed by $-CH_3/-CH_2$ groups (Table 2). The range of the H···O distances was 2.0-2.3 Å for the N−H···O hydrogen bonds, whereas for the C−H···O hydrogen bonds this range was 2.2−2.6 Å.

The literature provides no relevant experimental data on the geometry of hydrogen bonds in organo-clays and only some results can be found in the theoretical papers. Heinz *et al.* (2007) published FF-based data on hydrogen bonding for $R-NH_3^+$ surfactants on montmorillonite and mica with an average N−H···O distance of 1.5 Å. According to this value, these hydrogen bonds should be classified as strong. However, results from the DFT study did not confirm such short hydrogen bonding. For the *n*BAMnt models, distances obtained for N−H···O in the range of 2.0-2.5 Å (Table 2) classify these bonds as relatively weak. Heinz *et al.* (2007) also published results for $R-N(CH_3)_3^+$ surfactants obtaining an average H···O distance of 2.9 Å. The DFT calculations here resulted in C−H···O distances in the range 2.2-2.9 Å, depending on the type of the *n*BA cation (Table 2). The results, thus, also showed that $-CH_3/-CH_2$ groups can form weak hydrogen bonds and these results differ in some respects from those published by Heinz *et al.* (2007), especially for N−H···O bonding. This discrepancy can be assigned to the inaccuracy of the force field used in the work by Heinz *et al.* (2007).

The weakest C−H···O hydrogen bonds were found for the *4*BAMnt model (2.7−2.9 Å) (Scholtzová *et al.*, 2014) and the H···O distances increased slightly and the D−H···O (D = donor = N, C) angles also had a larger variation in comparison to the Mnt intercalated with tetramethylammonium (TMA-M) model in the work by Scholtzová *et al.* (2013). The calculated hydrogen bond angles (D−H···O, Table 2) indicate that some hydrogen bonds were not optimal (D−H···O < 150º), mainly due to steric factors and imperfect matching of the organic cations distributed in the interlayer space with the surface pattern of the basal oxygen atoms. A further observation is that in the case of the *1*BAMnt cation, one NH bond was not involved in hydrogen bonding.

In order to show a difference in the energetic stability of NaMnt and *n*BAMnt structures, the reaction energy for the exchange of the hydrated $[Na(H_2O)_6]^+$ by *n*BA cations was estimated using the reaction scheme NaMnt + nBA$^+$ → *n*BAMnt + $[Na(H_2O)_6]^+$. The energetic gain (ΔE_r in Table 1) documents the thermodynamic stability of all *n*BAMnt models. The stability decreased with the increasing number of butyl chains in order *1*BAMnt > *2*BAMnt *cis* ≈ *2*BAMnt *trans* > *3*BAMnt > *4*BAMnt and correlated very well with type, number, and strength of hydrogen bonds (Table 2). The presence and strength of the N−H···O hydrogen bonds is crucial for the stability of *n*BA cations keyed in the interlayer space of

Table 2. Parameters of hydrogen bonds for *n*BAMnt models (*n* = 1−4). The three numbers for C−H···O hydrogen bonds represent lower limit, median, and upper limit. In the case of N−H···O hydrogen bonds, only one or two such bonds are found in the structures, D = donor = N, C atom.

Model	H-bond	H···O (Å)	D···O (Å)	D−H···O (º)
*1*BAMnt	N−H···O	2.01;2.37	3.04;2.83	168;105
	C−H···O	2.4;2.54;2.58	2.94;3.30;3.57	103;128;162
*2*BAMnt$_{cis}$	N−H···O	2.49;2.50	3.02;3.49	111;161
	C−H···O	2.48;2.58;2.6	3.10;3.59;3.66	113;152;163
*2*BAMnt$_{trans}$	N−H···O	1.97	2.96	158
	C−H···O	2.31;2.43;2.59	3.20;3.35;3.54	128;142;176
*3*BAMnt	N−H···O	2.28	3.22	149
	C−H···O	2.18;2.54;2.60	3.00;3.47;3.62	123;142;167
*4*BAMnt*	N−H···O	-	-	–
	C−H···O	2.75;2.84;2.91	3.52;3.58;3.65	116;124;157

* Scholtzova *et al.*, 2014

https://doi.org/10.1346/CCMN.2016.0640404 Published online by Cambridge University Press

montmorillonite. This assumption is confirmed by a large drop of ΔE_r (Table 1) from *1*BAMnt (three N–H···O hydrogen bonds) to *4*BAMnt (no N–H···O hydrogen bond) which accounted for ~64.2 kJ/mol while a difference between [*1*BAMnt and *2*BAMnt (both *cis* and *trans*)] and [*2*BAMnt and *3*BAMnt] was about 20–25 kJ/mol. This can be explained by a difference in estimated energies of N–H···O and C–H···O hydrogen bonds, respectively (Jeffrey, 1997). The energy of the N–H···O type bond can be in the range 4.2–16.7 kJ/mol, whereas C–H···O hydrogen bonds are much weaker (< 2.1 kJ/mol) (Steiner, 2002). The hydrogen bonds of the R-NH_x^+ are stronger, mainly due to the large portion of the Coulombic interactions coming from the positively charged head groups. On the other hand, van der Waals interactions dominate in weak C–H···O hydrogen bonds. The observed significant differences between types and strengths of the hydrogen bonds formed between organic cations and the montmorillonite layers can have a significant impact on interlayer and superficial mobility of surfactants and cleavage energies of organo-clays. An additional important factor can also be alkyl chain length. The effect of head group structure and chain length on cleavage energy was demonstrated by classical MD simulations (Fu and Heinz, 2010a, 2010b).

Infrared spectra

The IR spectra of NaMnt and *n*BAMnt demonstrated a pronounced variability in the XH (X = O, N, C) stretching region that depended on the character of the exchangeable cation (Figure 4). The NaMnt spectrum showed an OH stretching vibration (ν(OH)) signal at 3623 cm^{-1} due to structural OH groups from montmorillonite, and a broad band near 3420 cm^{-1} due to overlapping contributions from differently bonded water molecules adsorbed on KBr and/or montmorillonite inner and outer surfaces. The position of ν(OH) remained similar for organo-clays containing $-NH_x$ groups, but a slight shift to higher wavenumbers and a shoulder near 3687 cm^{-1} appeared for *4*BAMnt.

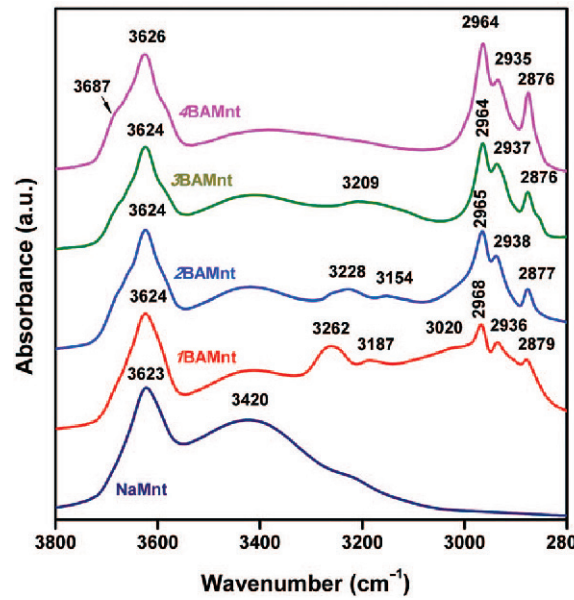

Figure 4. Experimental FTIR absorption spectra for NaMnt and *1*–*4*BAMnt samples – OH, NH, and CH stretching regions.

In addition to OH vibrations, the stretching CH and NH vibrations of the butylammonium cations in the spectra of organo-clays occur in the range of 3300–2800 cm^{-1} (Figure 4, Table 3). The spectrum of *1*BAMnt showed two bands at 3262 cm^{-1} and 3187 cm^{-1}, assigned to the ν_{as} and ν_s stretching vibrations of the $-NH_3$ group, respectively (Yariv, 2001). A broad shoulder with a weak maximum near 3020 cm^{-1} appeared in the spectrum of *1*BAMnt as well. The origin of this band has not been reported so far, but its position suggests that it might correspond to NH groups hydrogen-bonded to basal oxygens and/or to residual water molecules. This interpretation was supported by the calculated vibrational

Table 3. Frequencies (in cm^{-1}) and assignment of bands in experimental IR spectra of SAz-1 montmorillonite saturated with (*1*–*4*)-butylammonium cations.

*1*BAMnt	*2*BAMnt	*3*BAMnt	*4*BAMnt	Assignment
			3687	ν(OH)
3624	3624	3624	3626	ν(OH)
3262	3228			$\nu_{as}(NH_3^+)$, $\nu_{as}(NH_2^+)$
		3209		ν(NH)
3187	3154			$\nu_s(NH_3^+)$, $\nu_s(NH_2^+)$
3020				H-bonded $\nu_s(NH_3^+)$**
2968	2965	2964	2964	$\nu_{as}(CH_3)$
2936	2938	2937	2935	$\nu_{as}(CH_2)$
2879	2877	2876	2876*	$\nu_s(CH_3)$
2852*	2852*	2852*	2853*	$\nu_s(CH_2)$

* wavenumbers obtained by 2nd derivative.
** assigned on the base of calculated spectrum.

https://doi.org/10.1346/CCMN.2016.0640404 Published online by Cambridge University Press

spectra (Figure 5). The lowest frequency (3186 cm^{-1}) of the three NH stretching modes of the model *1*BAMnt might correspond to the experimentally detected band at 3020 cm^{-1}.

In comparison with the spectrum of *1*BAMnt, the broadening, intensity decrease, and red shift of two NH stretching bands to lower positions (3228 cm^{-1} and 3154 cm^{-1}) was observed for the *2*BA cation, which contains an NH_2 group. A weak and broad band that appeared near 3200 cm^{-1} in the *3*BAMnt spectrum arose from the ν(NH) vibration. To obtain more band positions, the second derivatives of the spectra were calculated.

The most characteristic IR bands of organic surfactants are in the 3000−2800 cm^{-1} region due to the vibrations of the $-CH_3$ and $-CH_2$ groups (Yariv, 2001). While well resolved bands near 2965 and 2935 cm^{-1} were due to $\nu_{as}(CH_3)$ and $\nu_{as}(CH_2)$, respectively; the complex band near 2877 cm^{-1} involved vibrational contributions of both moieties, $\nu_s(CH_3)$ and $\nu_s(CH_2)$ (Table 3).

A comparison of the calculated (Figure 5) and experimental (Figure 4) spectra showed very good correspondence in all three sectors of the high-frequency region (3800−2800 cm^{-1}). The calculated spectra, however, did not have the broad band observed in the experimental spectra at ~3420 cm^{-1}, which was assigned to residual water in the samples as in the other *n*BAMnt models, no water molecules were present. Generally, the calculated frequencies were higher than the experimental as a consequence of the harmonic approximation used in the frequency calculations. Anharmonicity of the *X*H (*X* = O, N, C) stretching modes is relatively high and could account for 60−150 cm^{-1} of the difference (Balan *et al.*, 2007).

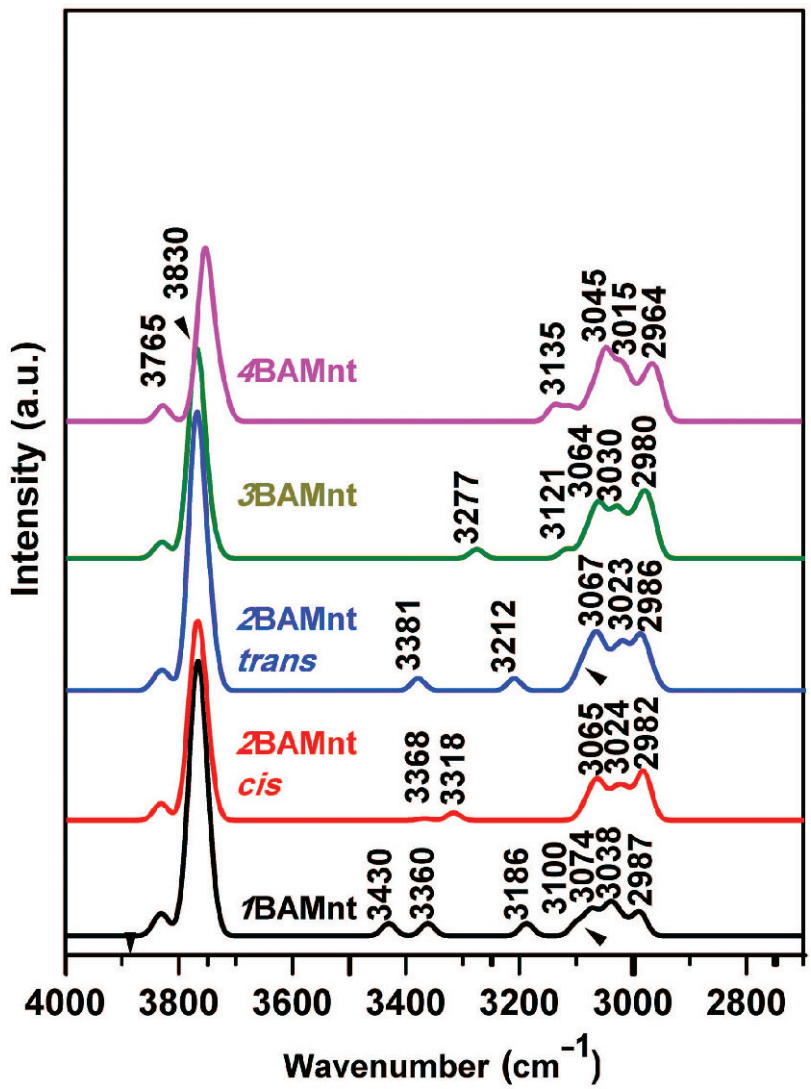

Figure 5. Calculated vibrational spectra for *1*−*4*BAMnt models − OH, NH, and CH stretching regions.

https://doi.org/10.1346/CCMN.2016.0640404 Published online by Cambridge University Press

Using an analysis of the eigenvectors of the calculated bands, exact assignment of all types of stretching modes was possible, and it was compared to the traditional interpretation of the experimental IR spectra.

The stretching vibrations of the montmorillonite inner −OH groups were clearly identified in the calculated spectrum (Figure 5). The bands at 3830 cm^{-1} were assigned to the Mg−OH stretching vibrations, whereas the bands at a lower energy (~3765 cm^{-1}) belonged to the Al−OH stretching vibrations. These bands were relatively stable for all models; only a small red shift (~10 cm^{-1}) was observed for the *4*BAMnt model. This shift could be related to the larger interlayer space expansion seen in the *4*BAMnt model in comparison to the *1*−*3*BAMnt models (Table 1). The usefulness of the calculated spectra was nicely demonstrated for the OH stretching modes. The calculated spectra clearly distinguished the Mg−OH and Al−OH stretching modes, whereas in the experimental spectra these bands overlapped to give only one broad band. The most visible Mg−OH stretching mode observed in the experiment was the shoulder seen at ~3687 cm^{-1} in the *4*BAMnt spectrum (Figure 4).

In the 3500−3100 cm^{-1} region of the calculated spectra, NH stretching vibrations were unambiguously identified (Figure 5). The *1*BAMnt spectrum had three NH stretching modes, corresponding to signals in the experimental spectrum at 3262, 3187, and 3020 cm^{-1} (Figure 4). The calculated band with the highest energy (3430 cm^{-1}) represented the NH stretching vibration of the free −NH group which was not involved in hydrogen bonding to the surface oxygen atoms of the layer. The second calculated band at 3360 cm^{-1} was assigned to the symmetric stretching vibration of the free −NH group and of one −NH group involved in hydrogen bonding, and corresponded to the band in the experimental spectrum at 3187 cm^{-1}. The third calculated band at 3186 cm^{-1} was the symmetric stretching vibration of the second −NH group, which was involved in the shortest hydrogen bond (2.01Å, Table 2), and corresponded to a broad, poorly distinguishable experimental peak at 3020 cm^{-1}. Theoretical calculations revealed that the two stretching vibrations of the $-NH_3$ group at (3430 and 3360 cm^{-1}) were decoupled due to different H-bonding environments of the two hydrogens, and also indicated that the weak experimental signal at 3020 cm^{-1} was the third $-NH_3$ stretching mode.

Both *cis* and *trans* *2*BAMnt models had calculated spectra with two well resolved NH stretching bands (Figure 5) that had a good correspondence with the bands at 3228 and 3154 cm^{-1} in the experimental spectrum (Figure 4). The band with the highest energy represented the asymmetric stretching vibration, whereas the second band represented the symmetric stretching vibration of the $-NH_2$ group. The calculated spectra of the *2*BAMnt *cis* and *trans* models showed a difference in the position and intensity of the NH stretching vibrations as a consequence of the different strengths of the corresponding N−H···O hydrogen bonds (Figure 5, Table 2). This assignment was consistent with the interpretation of the *2*BAMnt sample experimental spectrum (Table 3). Unfortunately, with the FTIR technique, distinguishing *cis* and *trans* configuration of butyl chains is not possible because of small (low intensity) and broad NH stretching mode peaks on a nonlinear background (Figure 4). Moreover, the experimental samples probably contained a mixture of *cis* and *trans* configurations in some ratio which can result in a superposition of the corresponding NH vibrational modes for these conformations in *2*BA.

For the *3*BAMnt model, only one NH stretching mode was calculated with a frequency of 3277 cm^{-1}. This band also corresponded to a feature of the experimental *3*BAMnt spectrum (Figure 4), a broad band with a maximum at 3209 cm^{-1}. The calculated frequency for this mode was higher than the lowest NH frequency of the *1*BAMnt model (3187 cm^{-1}), demonstrating different strengths of the N−H···O hydrogen bonds.

The CH stretching vibrations are predominantly found in the 3000−2800 cm^{-1} region. The analysis of the calculated spectrum of the *4*BAMnt model (Scholtzová *et al.*, 2014) showed that $-CH_3$ and $-CH_2$ vibrations had nearly identical energies, in the following order $-\nu_{as}(CH_3$ and $CH_2) > \nu_{as}(CH_3) > \nu_s(CH_2) > \nu_s(CH_3)$. This assignment was in disagreement with the standard assignment based on the experimental spectra, in which asymmetric stretching vibrations of the $-CH_3$ groups were higher than asymmetric stretching vibrations of the $-CH_2$ groups (Table 3). The MD simulations of the TEA-M model (Scholtzová *et al.*, 2014) revealed that the CH stretching vibration positions were sensitive to the $_{d001}$ spacing, which could lead to a reordering of the CH stretching modes.

The vibrational analysis of the calculated spectra of the *1*-*3*BAMnt model was similar to that of the *4*BAMnt spectrum (Figure 5). The slightly higher positions of all ν(CH) in the *1*−*3*BAMnt models than in the *4*BAMnt model could result from the vicinity of the $-NH_x$ groups to the $-CH_3$ and $-CH_2$ groups (Vaia *et al.*, 1994). The discovered CH_3/CH_2 stretching mode order for the *1*−*3*BAMnt models was: $\nu_{as}(CH_2) > \nu_{as}(CH_3) > \nu_s(CH_3+CH_2) > \nu_s(CH_3)$ for the *1*BAMnt and *2*BAMnt *trans* models, and $\nu_{as}(CH_2) > \nu_{as}(CH_3) > \nu_s(CH_3+CH_2) > \nu_s(CH_2)$ for the *2*BAMnt *cis* and *3*BAMnt models (Table 4). The difference in the order between the two *2*BAMnt models indicated a high sensitivity of the CH_3/CH_2 stretching modes to the arrangement and relative positions of the alkyl chains in the monolayer quasi-planar configuration in the montmorillonite interlayer space.

The CH_3 and CH_2 stretching vibration bands in the calculated spectra had a more complicated structure than the corresponding experimental bands, and had some shoulders at the high frequency edge. These shoulders

https://doi.org/10.1346/CCMN.2016.0640404 Published online by Cambridge University Press

Table 4. Assignment and ordering of calculated CH_2/CH_3 stretching vibrations of *1*–*4*BAMnt models.

Models	Assignment/wavenumber (cm^{-1})			
*1*BAMnt	$\nu_{as}(CH_2)$ 3100	$\nu_{as}(CH_3)$ 3060	$\nu_s(CH_3+CH_2)$ 3036	$\nu_s(CH_3)$ 2987
*2*BAMnt$_{cis}$	$\nu_{as}(CH_2)$ 3088	$\nu_{as}(CH_3)$ 3062	$\nu_s(CH_3+CH_2)$ 3018	$\nu_s(CH_2)$ 2979
*2*BAMnt$_{trans}$	$\nu_{as}(CH_2)$ 3100	$\nu_{as}(CH_3)$ 3066	$\nu_s(CH_3+CH_2)$ 3017	$\nu_s(CH_3)$ 2984
*3*BAMnt	$\nu_{as}(CH_2)$ 3120	$\nu_{as}(CH_3)$ 3057	$\nu_s(CH_3+CH_2)$ 3025	$\nu_s(CH_2)$ 2977
*4*BAMnt	$\nu_{as}(CH_3+CH_2)$ 3135	$\nu_{as}(CH_3)$ 3045	$\nu_s(CH_2)$ 3015	$\nu_s(CH_3)$ 2970

were assigned to the vibrations of the individual groups which were involved in the hydrogen bonds. In the experimental spectrum, these shoulders were not distinguished (Figure 4). The bands in the experimental spectra were broadened and strongly overlapped and complete and unambiguous assignment was somewhat difficult.

Several factors impacted the band broadening. The arrangement and the distribution of the organic cations in the monolayer configuration were not perfectly regular in the samples (in contrast to the regular periodic models in the simulation). Further, the samples could still contain some residual interlayer or surface water in spite of the overnight heating (*e.g.* 1.3 wt.% water was detected in the *4*BAMnt sample). Residual water molecules, thus, can disturb NH and CH vibrations. The sample particles are usually <2 μm in size (Tributh and Lagaly, 1986), and significant contributions from the edge surfaces and edge effects are expected. Indeed, the calculations on the structural models have an advantage as these complicating effects are not involved in the models and the structure and interactions of the organic cations in the interlayer space can be analyzed in isolation.

CONCLUSIONS

The DFT calculations showed that the optimized structures of the *n*BAMnt models had a nearly planar arrangement of the *n*-butylammonium cations (n = 1–4) and that the basal spacing d_{001} increased only slightly with increasing size of the cation. The calculated values corresponded well with the XRD-determined d_{001} values of the experimental samples.

Hydrogen bonds play an important role in the arrangement and stabilization of interlayer cations combined with the electrostatic interactions between montmorillonite layers and intercalated organic cations. The *n*BA cations form moderate-to-weak N–H···O and weak C–H···O hydrogen bonds between $-NH_x/-CH_2/-CH_3$ groups and basal oxygen atoms of the montmorillonite layers. Some of the bonds are not optimally formed due to steric factors.

Calculated exchange reaction energies showed the thermodynamic stability of all models that increased from *4*BAMnt to *1*BAMn. The analysis of the exchange reaction energies documented the importance of the N–H···O hydrogen bonds in the stability of the organic cations in the interlayer space of montmorillonite.

The calculated vibrational spectra of the *n*BAMnt models showed good correspondence with the experimental FTIR spectra. Unambiguous assignment of the NH_x and CH_2/CH_3 stretching bands to individual types of vibrations was performed on the basis of the calculated spectra and was compared to traditional interpretations of the experimental bands. Very good agreement was found between calculated and experimental NH_x stretching modes. On the basis of the calculated spectrum of the *1*BAMnt model, a possible interpretation was suggested for the poorly resolved band at 3020 cm^{-1}. The calculated vibrational spectra showed a small shift of the CH_2/CH_3 stretching modes to lower values with increasing number of butyl chains in the *n*BA cation. The order of the CH_2/CH_3 stretching modes, however, was not always identical for all models. The observed changes of the CH stretching vibration bands indicate that CH_2/CH_3 stretching modes are very sensitive to the local environment. These tiny effects were not distinguishable from the experimental spectra and could be analyzed only from the calculated spectra.

ACKNOWLEDGMENTS

The financial support of the Slovak Grant Agency VEGA (Grant 2/0132/13) is gratefully acknowledged. DT also acknowledges the support by the Austrian Science Fund (FWF), project number I880-N21, and CPU time at the Vienna Scientific Cluster (VSC), project number 70544. Part of the calculations were also performed at

the Computing Center of the Slovak Academy of Sciences using the supercomputing infrastructure acquired in projects ITMS 26230120002 and 26210120002 (Slovak infrastructure for high-performance computing) supported by the Research and Development Operational Programme funded by the ERDF. H. Pálková is thanked for IR spectra measurements.

REFERENCES

Aggarwal, V., Chien, Y.Y., and Teppen, B.J. (2007) Molecular simulations to estimate thermodynamics for adsorption of polar organic solutes to montmorillonite. *European Journal of Soil Science*, **58**, 945–957.

Balan, E., Lazzeri, M., Delattre, S., Meheut, M., Refson, K., and Winkler, B. (2007) Anharmonicity of inner-OH stretching modes in hydrous phyllosilicates: assessment from first-principles frozen-phonon calculations. *Physics and Chemistry of Minerals*, **34**, 621–625.

Berghout, A., Tunega, D., and Zaoui, A. (2010) Density functional theory (DFT) study of the hydration steps of Na^{+}/Mg^{2+}/Ca^{2+}/Sr^{2+}/Ba^{2+}-exchanged montmorillonites. *Clays and Clay Minerals*, **58**, 174–187.

Bhattacharyya, K.G. and Sen Gupta, S. (2006) Kaolinite, montmorillonite, and their modified derivatives as adsorbents for removal of Cu(II) from aqueous solution. *Separation and Purification Technology*, **50**, 388–397.

Bhattacharyya, K.G. and Sen Gupta, S. (2009) Calcined tetrabutylammonium kaolinite and montmorillonite and adsorption of Fe(II), Co(II) and Ni(II) from solution. *Applied Clay Science*, **46**, 216–221.

Blochl, P.E. (1994) Projector augmented-wave method. *Physical Review B*, **50**, 17953-17979.

Breen, C., Watson, R., Madejová, J., Komadel, P., and Klapyta, Z. (1997) Acid-activated organoclays: Preparation, characterization and catalytic activity of acid-treated tetraalkylammonium-exchanged smectites. *Langmuir*, **13**, 6473–6479.

Chun, Y., Sheng, G.Y., and Boyd, S.A. (2003) Sorptive characteristics of tetraalkylammonium-exchanged smectite clays. *Clays and Clay Minerals*, **51**, 415–420.

Czimerova, A., Ceklovsky, A., and Bujdak, J. (2009) Interaction of montmorillonite with phenothiazine dyes and pyronin in aqueous dispersions: A visible spectroscopy study. *Central European Journal of Chemistry*, **7**, 343–353.

de Paiva, L.B., Morales, A.R., and Valenzuela Diaz, F.R. (2008) Organoclays: Properties, preparation and applications. *Applied Clay Science*, **42**, 8–24.

Desiraju, G.R. and Steiner, T. (2006) *The Weak Hydrogen Bond in Structural Chemistry and Biology* 2nd Edition. Oxford University Press, Oxford, UK.

Frost, R.L., Zhou, Q., He, H., and Xi, Y. (2008) An infrared study of adsorption of para-nitrophenol on mono-, di- and tri-alkyl surfactant intercalated organoclays. *Spectrochimica Acta Part A – Molecular and Biomolecular Spectroscopy*, **69**, 239–244.

Fu, Y.-T. and Heinz, H. (2010a) Cleavage energy of alkylammonium-modified montmorillonite and relation to exfoliation in nanocomposites: Influence of cation density, head group structure, and chain length. *Chemistry of Materials*, **22**, 1595–1605.

Fu, Y.-T. and Heinz, H. (2010b) Structure and cleavage energy of surfactant-modified clay minerals: Influence of CEC, head group and chain length. *Philosophical Magazine*, **90**, 2415–2424.

Ghiaci, M., Kalbasi, R.J., and Sedaghat, M.E. (2003) A kinetic study of 2-ethyl-1-hexanol oxidation by dichromate using clay-supported 1-butyl 4-aza-1-azonia bicyclo 2.2.2 octane chloride as the phase-transfer catalyst. *Organic Process Research & Development*, **7**, 936–938.

Guegan, R. (2010) Intercalation of a nonionic surfactant (C10E3) bilayer into a Na-montmorillonite clay. *Langmuir*, **26**, 19175–19180.

Guegan, R. (2013) Self-assembly of a non-ionic surfactant onto a clay mineral for the preparation of hybrid layered materials. *Soft Matter*, **9**, 10913–10920.

Hafner, J. (2003) Vibrational spectroscopy using ab initio density-functional techniques. *Journal of Molecular Structure*, **651-653**, 3–17.

He, H., Frost, R.L., Xi, Y.F., and Zhu, J.X. (2004) Raman spectroscopic study of organo-montmorillonites. *Journal of Raman Spectroscopy*, **35**, 316–323.

He, H., Ma, L., Zhu, J., Frost, R.L., Theng, B.K.G., and Bergaya, F. (2014) Synthesis of organoclays: A critical review and some unresolved issues. *Applied Clay Science*, **100**, 22–28.

Heinz, H., Koerner, H., Anderson, K.L., Vaia, R.A., and Farmer, B.L. (2005) Force field for mica-type silicates and dynamics of octadecylammonium chains grafted to montmorillonite. *Chemistry of Materials*, **17**, 5658–5669.

Heinz, H., Vaia, R.A., Krishnamoorti, R., and Farmer, B.L. (2007) Self-assembly of alkylammonium chains on montmorillonite: Effect of chain length, head group structure, and cation exchange capacity. *Chemistry of Materials*, **19**, 59–68.

Jankovic, L., Kronek, J., Madejova, J., and Hronsky, V. (2015) (9,10-Dihydroxyoctadecyl)ammonium: A structurally unique class of clay intercalable surfactants. *European Journal of Inorganic Chemistry*, 2841–2850.

Jeffrey, G.A. (1997) *An Introduction to Hydrogen Bonding*. Oxford University Press: New York.

Klebow, B. and Meleshyn, A. (2012) Monte Carlo Study of the Adsorption and Aggregation of Alkyltrimethylammonium Chloride on the Montmorillonite-Water Interface. *Langmuir*, **28**, 13274–13283.

Kresse, G. and Furthmuller, J. (1996) Efficient iterative schemes for ab initio total-energy calculations using a plane-wave basis set. *Physical Review B*, **54**, 11169–11186.

Kresse, G. and Hafner, J. (1993) Ab-initio molecular-dynamics for open-shell transition-metals. *Physical Review B*, **48**, 13115–13118.

Kresse, G. and Joubert, D. (1999) From ultrasoft pseudopotentials to the projector augmented-wave method. *Physical Review B*, **59**, 1758–1775.

Kukkadapu, R.K. and Boyd, S.A. (1995) Tetramethylphosphonium-smectite and tetramethylammonium-smectite as adsorbents of aromatic and chlorinated hydrocarbons - effect of water on adsorption efficiency. *Clays and Clay Minerals*, **43**, 318–323.

Lagaly, G., Ogawa, M., and Dékány, I. (2006) Chapter 7.3 Clay Mineral Organic Interactions. **1**, 309–377.

Lawrence, M.A.M., Kukkadapu, R.K., and Boyd, S.A. (1998) Adsorption of phenol and chlorinated phenols from aqueous solution by tetramethylammonium- and tetramethylphosphonium-exchanged montmorillonite. *Applied Clay Science*, **13**, 13–20.

Lee, J.F., Mortland, M.M., Chiou, C.T., Kile, D.E., and Boyd, S.A. (1990) Adsorption of benzene, toluene, and xylene by 2 tetramethylammonium-smectites having different charge-densities. *Clays and Clay Minerals*, **38**, 113–120.

Madejová, J., Palkova, H., and Komadel, P. (2010) IR spectroscopy of clay minerals and clay nanocomposites. Pp. 22–71 in: *Spectroscopic Properties of Inorganic and Organometallic Compounds: Techniques, Materials and Applications, Volume*, **41** (J. Yarwood, R. Douthwaite, and S.B. Duckett, editors). The Royal Society of Chemistry, Cambridge, UK.

Madejová, J., Pálková, H., and Jankovič, L'. (2012) Degradation of surfactant-modified montmorillonites in

HCl. *Materials Chemistry and Physics*, **134**, 768–776.
Pálková, H., Jankovič, L'., Zimowska, M., and Madejová, J. (2011) Alterations of the surface and morphology of tetraalkyl-ammonium modified montmorillonites upon acid treatment. *Journal of Colloid and Interface Science*, **363**, 213–222.
Palkova, H., Hronsky, V., Jankovič, L'., and Madejová, J. (2013) The effect of acid treatment on the structure and surface acidity of tetraalkylammonium-montmorillonites. *Journal of Colloid and Interface Science*, **395**, 166–175.
Perdew, J.P., Burke, K., and Wang, Y. (1996) Generalized gradient approximation for the exchange-correlation hole of a many-electron system. *Physical Review B*, **54**, 16533–16539.
Raussell-Colom, J.A. and Serratosa, J.M. (1987) Reactions of clays with organic substances. Pp. 371–422 in: *Chemistry of Clays and Clay Minerals* (A.C.D. Newman, editor). Longman Scientific and Technical, Essex, UK.
Ruiz-Hitzky, E. and Van Meerbeek, A. (2006) Clay mineral- and organoclay-polymer nanocomposite. Pp. 583–621 in: *Handbook of Clay Science*, **1** (F. Bergaya, B.K.G. Theng, and G. Lagaly, editors). Developments in Clay Science. Elsevier.
Sen Gupta, S. and Bhattacharyya, K.G. (2005) Interaction of metal ions with clays: I. A case study with Pb(II). *Applied Clay Science*, **30**, 199–208.
Sen Gupta, S. and Bhattacharyya, K.G. (2006) Removal of Cd(II) from aqueous solution by kaolinite, montmorillonite and their poly(oxo zirconium) and tetrabutylammonium derivatives. *Journal of Hazardous Materials*, **128**, 247–257.
Seyidoğlu, T. and Yilmazer, U. (2013) Modification and characterization of bentonite with quaternary ammonium and phosphonium salts and its use in polypropylene nanocomposites. *Journal of Thermoplastic Composite Materials*, **28**, 86–110.
Scholtzova, E. and Smrcok, L. (2009) Hydrogen bonding and vibrational spectra in kaolinite-dimethylsulfoxide and -dimethylselenoxide intercalates – a solid-state computational study. *Clays and Clay Minerals*, **57**, 54–71.
Scholtzova, E., Benco, L., and Tunega, D. (2008) A model study of dickite intercalated with formamide and N-methylformamide. *Physics and Chemistry of Minerals*, **35**, 299–309.
Scholtzová, E., Tunega, D., Madejová, J., Pálková, H., and Komadel, P. (2013) Theoretical and experimental study of montmorillonite intercalated with tetramethylammonium cation. *Vibrational Spectroscopy*, **66**, 123–131.
Scholtzová, E., Madejová, J., and Tunega, D. (2014) Structural properties of montmorillonite intercalated with tetraalkyl-ammonium cations – Computational and experimental study. *Vibrational Spectroscopy*, **74**, 120–126.
Steiner, T. (2002) The hydrogen bond in the solid state. *Angewandte Chemie (International ed. in English)*, **41**, 49–76.
Stevens, J.J. and Anderson, S.J. (1996) Orientation of trimethylphenylammonium (TMPA) on Wyoming montmorillonite: Implications for sorption of aromatic compounds. *Clays and Clay Minerals*, **44**, 132–141.
Sun, L.L., Tanskanen, J.T., Hirvi, J.T., Kasa, S., Schatz, T., and Pakkanen, T.A. (2015) Molecular dynamics study of montmorillonite crystalline swelling: Roles of interlayer cation species and water content. *Chemical Physics*, **455**, 23–31.
Szczerba, M., Klapyta, Z., and Kalinichev, A. (2014) Ethylene glycol intercalation in smectites. Molecular dynamics simulation studies. *Applied Clay Science*, **91-92**, 87–97.
Teppen, B.J., Yu, C.H., Miller, D.M., and Schafer, L. (1998) Molecular dynamics simulations of sorption of organic compounds at the clay mineral aqueous solution interface. *Journal of Computational Chemistry*, **19**, 144–153.
Theng, B.K.G. (1974) *The Chemistry of Clay-Organic Reactions.* Adam Hilger, London.
Tributh, H. and Lagaly, G. (1986) Aufbereitung und Identifizierung von Boden- und Lagerstättentonen. *GIT Labor-Fachzeitschrift*, **30**, 524–529.
Tsipurski, S.I. and Drits, V.A. (1984) The distribution of octahedral cations in the 2:1 layers of dioctahedral smectites studied by oblique-texture electron diffraction. *Clay Minerals*, **19**, 177–193.
Vaia, R.A., Teukolsky, R.K., and Giannelis, E.P. (1994) Interlayer structure and molecular environment of alkylammonium layered silicates. *Chemistry of Materials*, **6**, 1017–1022.
Wibowo, T.Y., Abdullah, A.Z., and Zakaria, R. (2010) Organo-montmorillonites as catalysts for selective synthesis of glycerol monolaurate. *Applied Clay Science*, **50**, 280–281.
Yariv, S. (2001) IR spectroscopy and Thermo-IR spectroscopy in the study of the fine structure of organo-clay complexes. Pp. 345–462 in: *Organo-Clay Complexes and Interactions*. (S. Yariv and H. Cross). Marcel Dekker, Inc, New York.
Zhu, J.X., He, H.P., Zhu, L.Z., Wen, X.Y., and Deng, F. (2005) Characterization of organic phases in the interlayer of montmorillonite using FTIR and C-13 NMR. *Journal of Colloid and Interface Science*, **286**, 239-244.

(*Received 23 October 2015; revised 9 May 2016; Ms. 1055; AE: Xiandong Liu*)